Supporting Information for "Distinct C-tail dynamics between β-arrestin isoforms in forming GPCR tail- and core-engaged complexes"

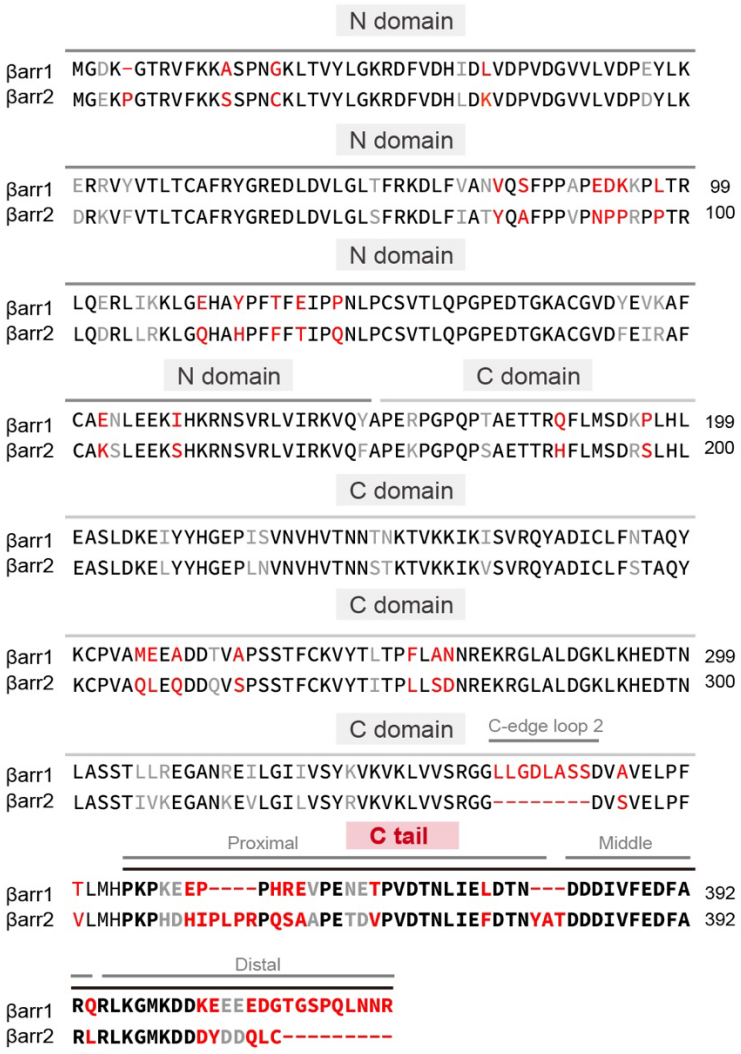

Fig. S1. Sequence comparison between human βarr1 and βarr2 isoforms. Non-conserved amino acid differences between the two isoforms are colored in red, whereas identical and conserved residues are shown in black and gray, respectively.

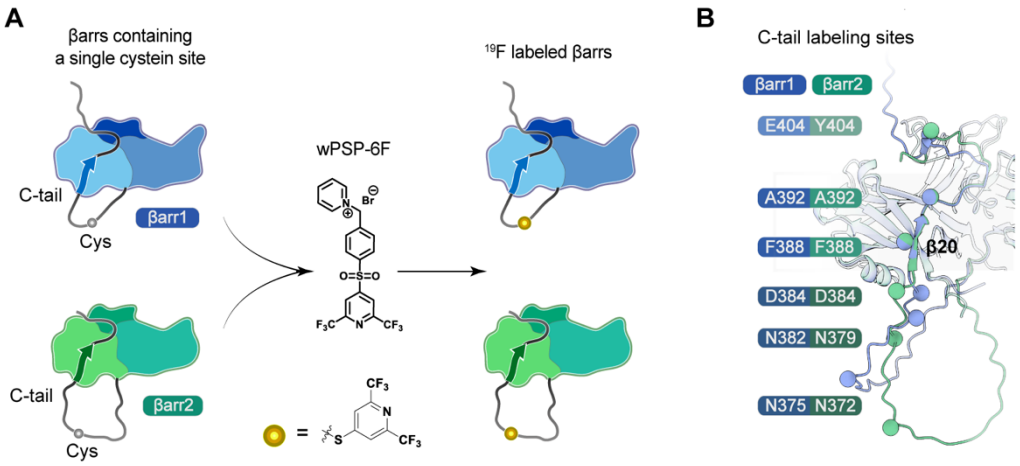

Fig. S2. ^{19}F-labeling scheme for βarr1 and βarr2. (A) A schematic illustration showing the single-site ^{19}F labeling of βarr1 and βarr2 using the wPSP-6F probe. (B) Locations of the equivalent labeling sites in the two βarr isoforms mapped onto the basal state structural models.

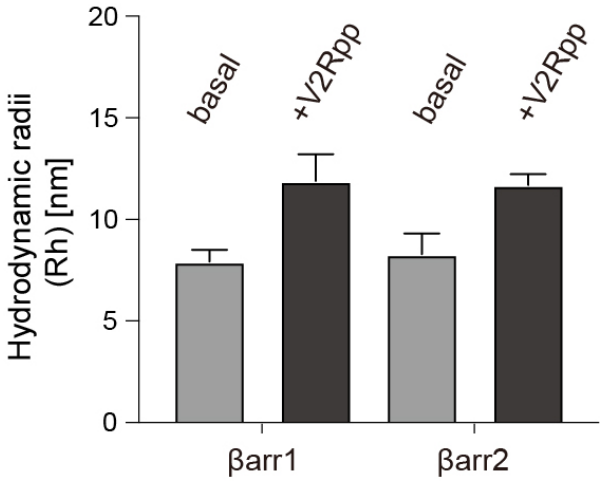

Fig. S3. Protein size assessment by dynamic light scattering (DLS). DLS measurements of the hydrodynamic radius (*Rh*) of βarrs (0.5 mg/mL) before and after adding V2Rpp. Data are presented as mean values ± SD of n = 7 technical replicates.

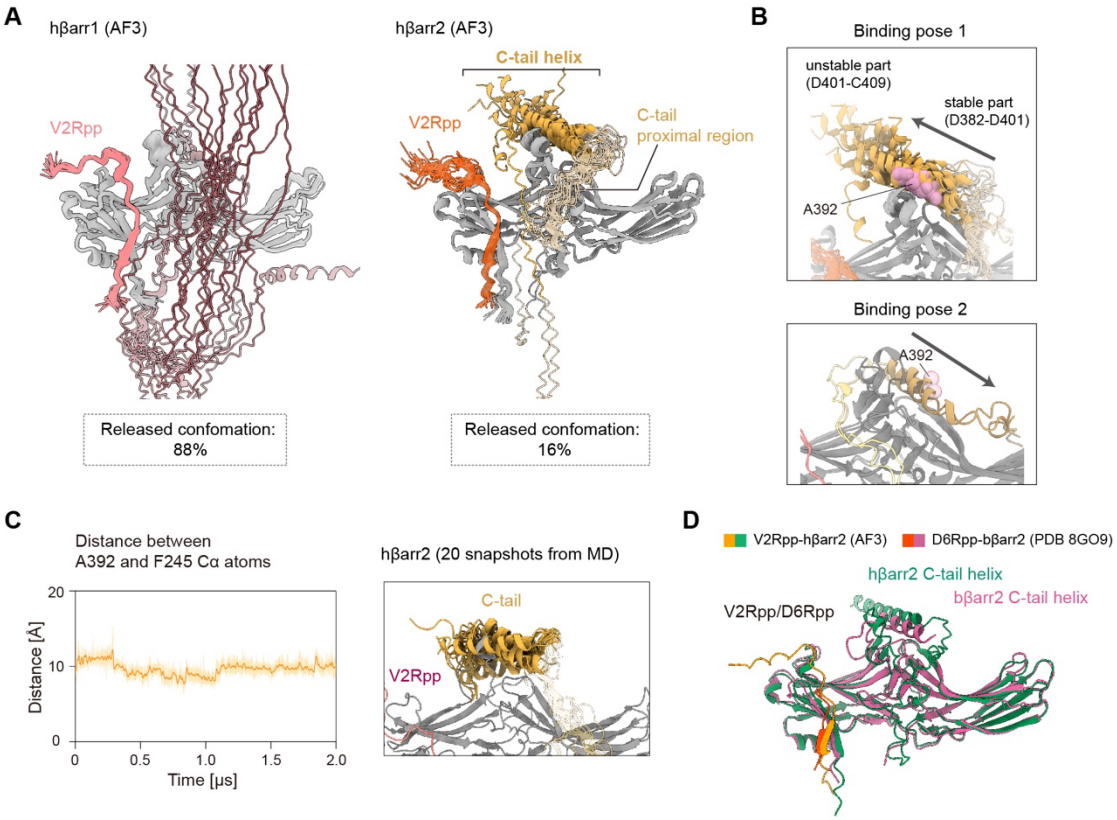

Fig. S4. AlphaFold3 predictions of V2Rpp-activated βarr structures. (**A**) Twenty randomly selected models of V2Rpp-complexed βarr1/2 structures from AF3 predictions (n_{model} = 92). The population of the conformations with a free released C-tail is calculated for both βarrs based on all 92 predictions. (**B**) Two different binding poses of the βarr2 C-tail helix observed in the AF3 predictions. (**C**) A time trace showing the fluctuations of the distance between the A392 (C-tail) and F245 (central crest C loop) Cα atoms in a 2 μs MD simulation of V2Rpp–βarr2 complex starting from an AF3 model (left), and an overlay of 20 conformational snapshots along the time trace at 100 ns intervals. (**D**) Overlay of the AF3-predicted V2Rpp–human βarr2 structure (major binding pose) with the experimentally determined D6Rpp–bovine βarr2 complex structure (PDB 8GO9). The Fab30 molecule in the D6Rpp–bovine βarr2 structure is omitted.

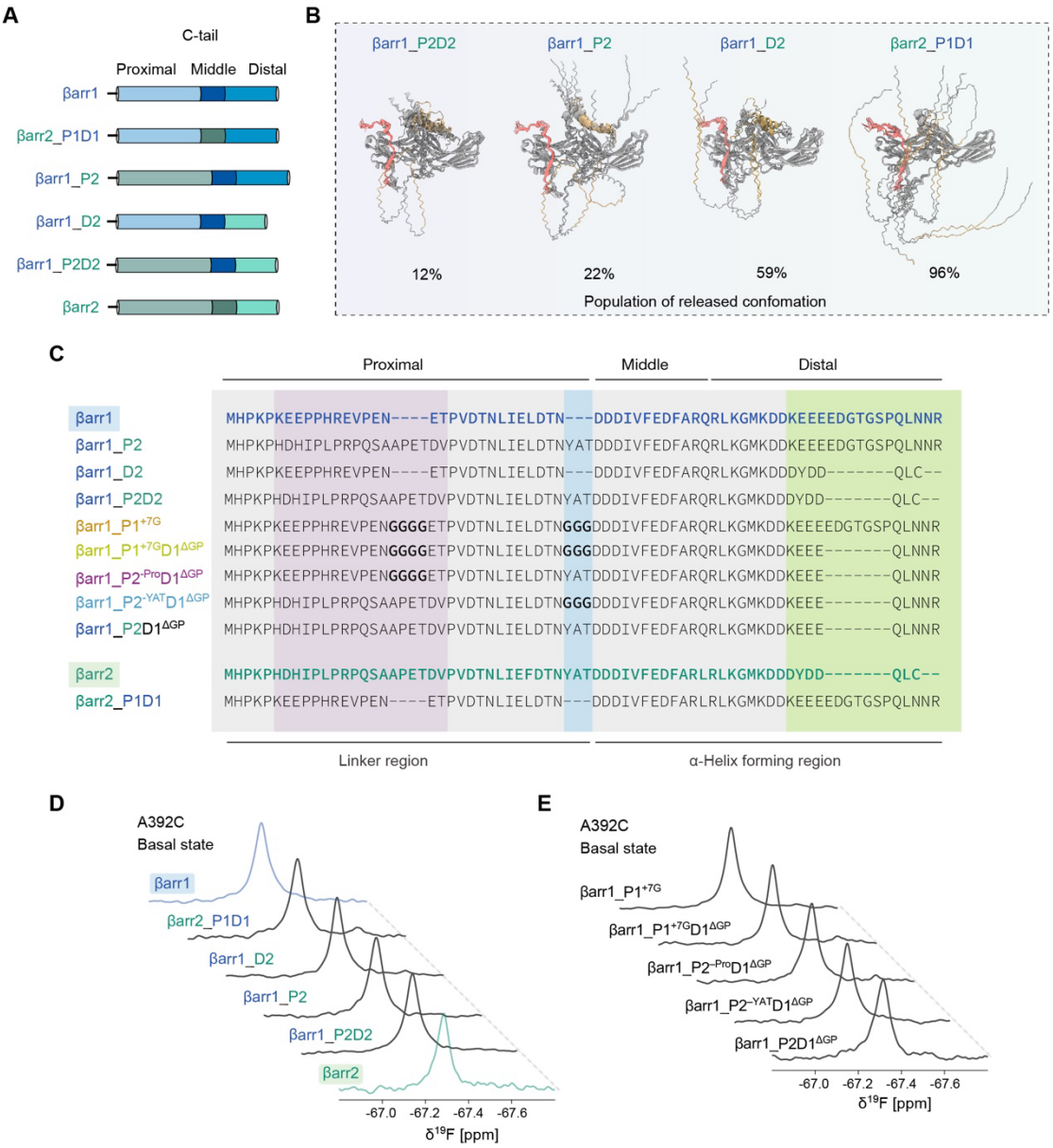

Fig. S5. Preparations of different βarr chimeras. (**A**) A schematic illustration of the construct design of βarr C-tail chimeras. (**B**) Five randomly selected models of βarr chimeras in the V2Rpp-complexed state from AF3 predictions (n_{model} = 92), with the C-tails colored in orange. The population of the conformations with a released C-tail is calculated based on all 92 predictions. (**C**) C-tail sequences of the βarrs mutants. Conserved regions are shown in gray, the proline-rich region in the proximal segment is shown in purple, the YAT motif is shown in blue, and the distal segment is shown in green. (**D-E**) The basal-state ^{19}F NMR spectra of the A392C site in βarr C-tail chimeras and additional βarr1 mutants.

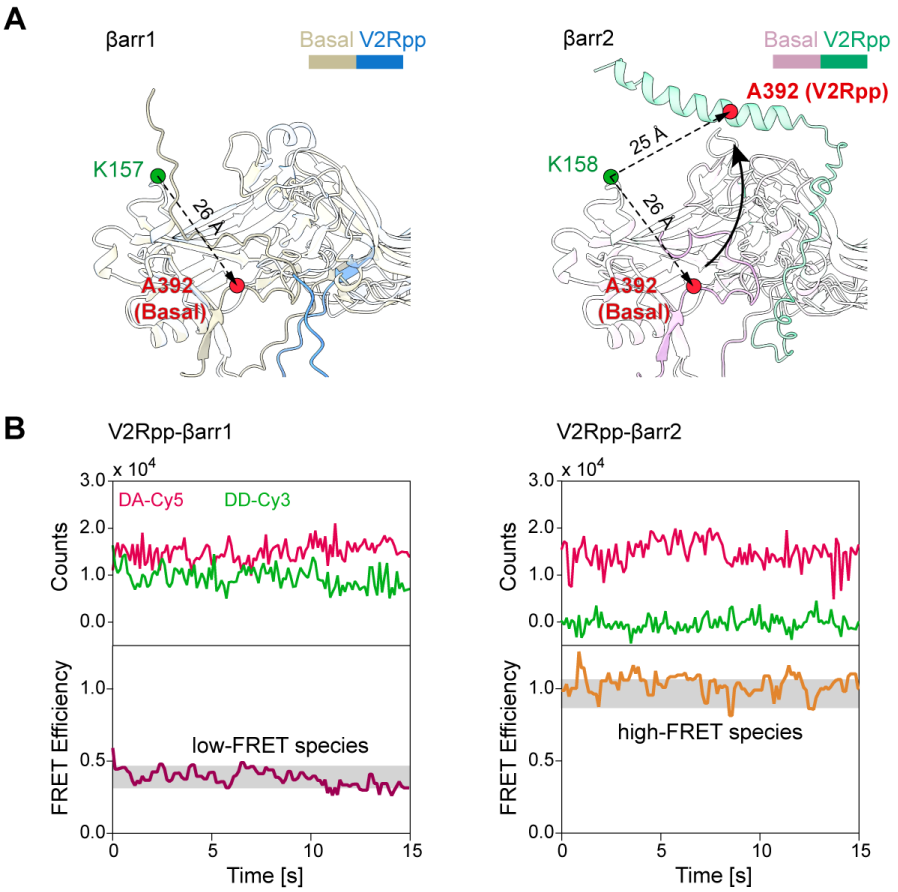

Fig. S6. smFRET reveals distinct C-tail conformations in βarr1 and βarr2. (**A**) Distances between the FRET sites in the basal state of βarr1 (left), and in both the basal and V2Rpp-activated states of βarr2 (right). (**B**) Representative single-molecule traces of the fluorescence (donor in green, acceptor in red) and FRET (bottom) results for both βarrs in the presence of 300 μM V2Rpp. The data were recorded using an objective-based TIRF microscope with 100 ms imaging.

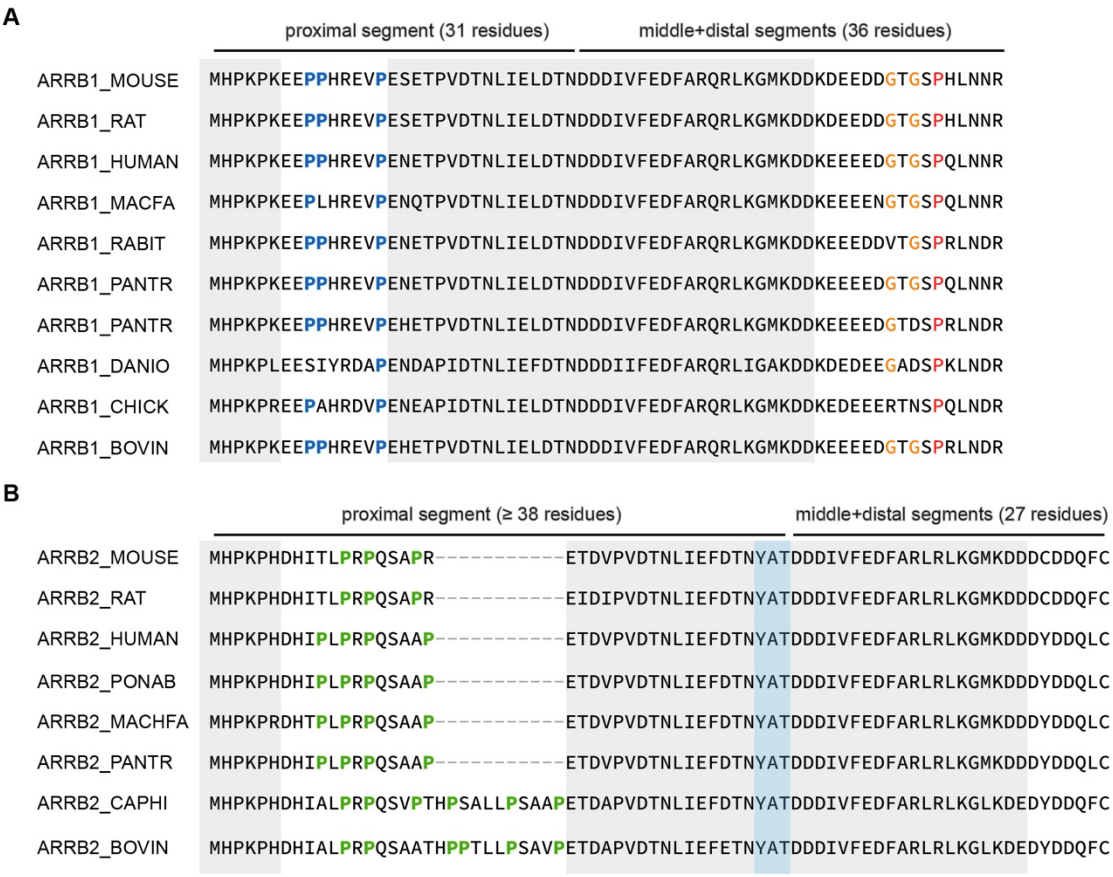

Fig. S7. C-tail sequence alignments of both βarr isoforms across different species. (**A**) Sequences of βarr1 were obtained from the UniProt database: Q8BWG8 (ARRB1_MOUSE), P29066 (ARRB1_RAT), P49407 (ARRB1_HUMAN), Q4R562 (ARRB1_MACFA), Q95223 (ARRB1_RABBIT), C3PTE8 (ARRB1_DANIO), A0A8V0XCX3 (ARRB1_CHICK), H2R1Z2 (ARRB1_PANTR), A0A452EHP7 (ARRB1_CAPHI), and P17870 (ARRB1_BOVIN). (**B**) Sequences of βarr2 were obtained from the UniProt database: Q91YI4 (ARRB2_MOUSE), P29067 (ARRB2_RAT), P32121 (ARRB2_HUMAN), A0A7N9D4J4 (ARRB2_MACFA), H2QBY1 (ARRB2_PANTR), A0A452ESR2 (ARRB2_CAPHI), and P32120 (ARRB2_BOVIN). The Pro-rich sequence in the proximal segment of βarr1/2, the Gly/Pro-rich sequence in the distal segment of βarr1, and the YAT motif in βarr2 are highlighted.

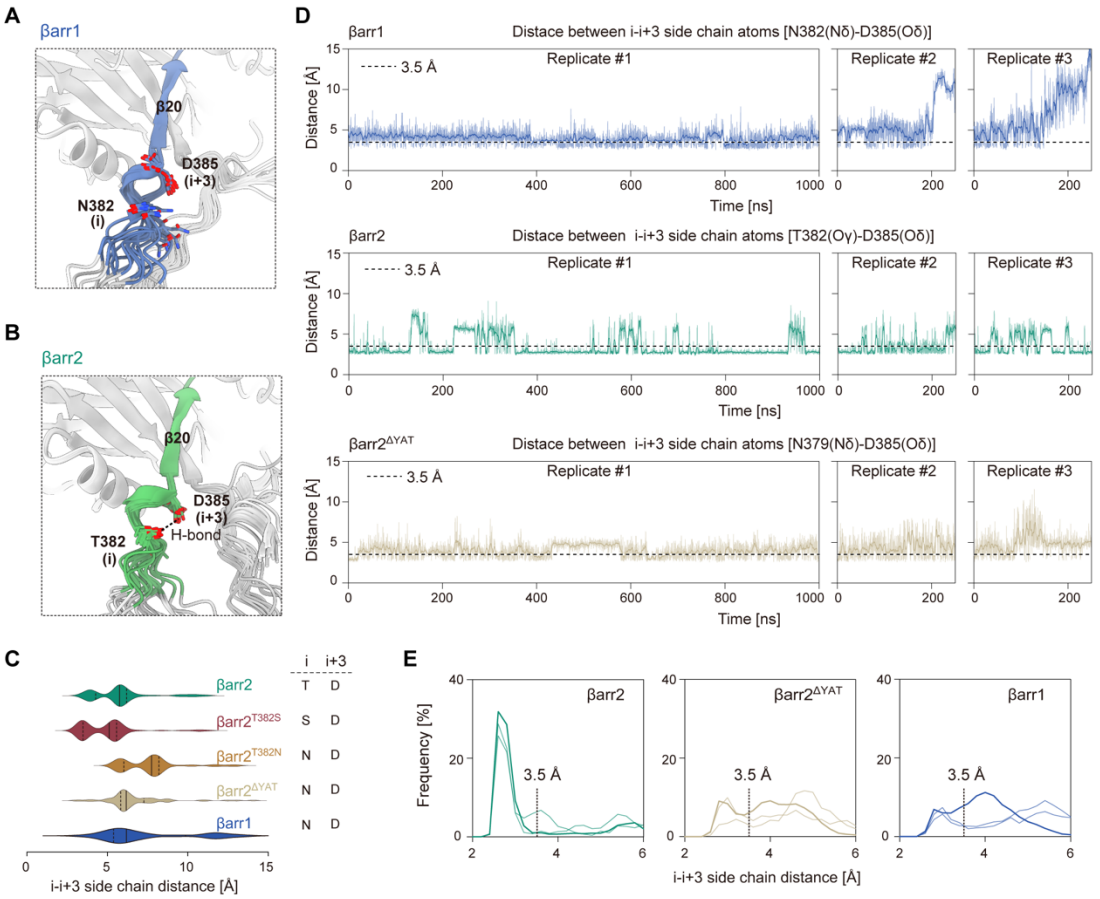

Fig. S8. Conformational analysis of the YAT motif by AF3 predictions and MD simulations. (**A**–**B**) AF3 models of full-length βarr1 (A) and βarr2 (B) in the basal state (20 models each), showing the local conformation of the N382/T382–D385 segment upstream of β20. The side chains of N382/T382 and D385 are shown in sticks. (**C**) Violin plots showing the distributions of the i→i+3 side chain distances (the i+3 position corresponds to D385 in both βarrs) in βarr1, βarr2 and βarr2 mutants computed from AF3 models (n_{model} = 80), with solid and dashed lines indicating the median and interquartile range. The distances were calculated between the Oδ atom of D385 (i+3) and the Oγ, Oβ or Nδ atoms of the Thr, Ser or Asn residues at the i position. (**D**) Time traces of basal-state βarr1, βarr2 and βarr2$^{\Delta YAT}$ showing the i→i+3 side chain distances (i+3 corresponds to D385) in three MD trajectories (traj 1: 1 μs, traj 2&3: 250 ns). All trajectories start from an initial state with a helical-like conformation at the 382–385 region. Dashed lines indicate the threshold of 3.5 Å, distance below which is favorable for hydrogen bond formation. (**E**) Frequency distributions of the i→i+3 distance computed from the time trances in (D). Thick and thin lines correspond to results from traj 1 and traj 2–3, respectively.

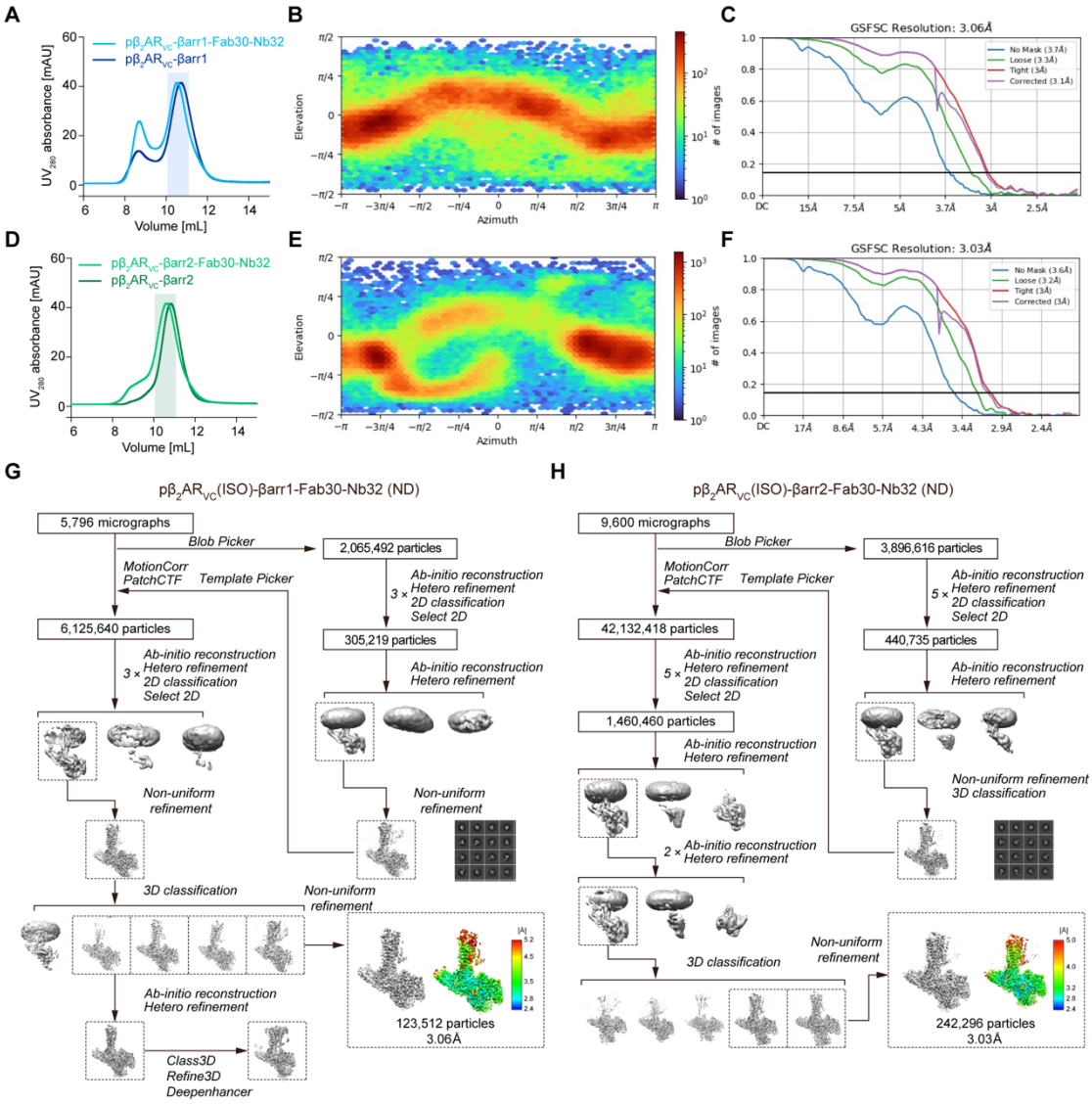

Fig. S9. Protein preparation, cryo-EM data-processing workflow, and resolution assessment for pβ2ARVC–βarr complexes. (**A–C**) pβ2ARVC–βarr1: size-exclusion chromatography (SEC) profile, angular plot of the particles used for 3D reconstruction, and gold-standard Fourier shell correlation (FSC) curves for the maps. (**D–F**) pβ2ARVC–βarr2: SEC profile, angular plot of the particles used for 3D reconstruction, and gold-standard FSC curves for the maps. (**G**) Cryo-EM data-processing workflow for the pβ2ARVC–βarr1 complex. (**H**) Cryo-EM data-processing workflow for the pβ2ARVC–βarr2 complex.

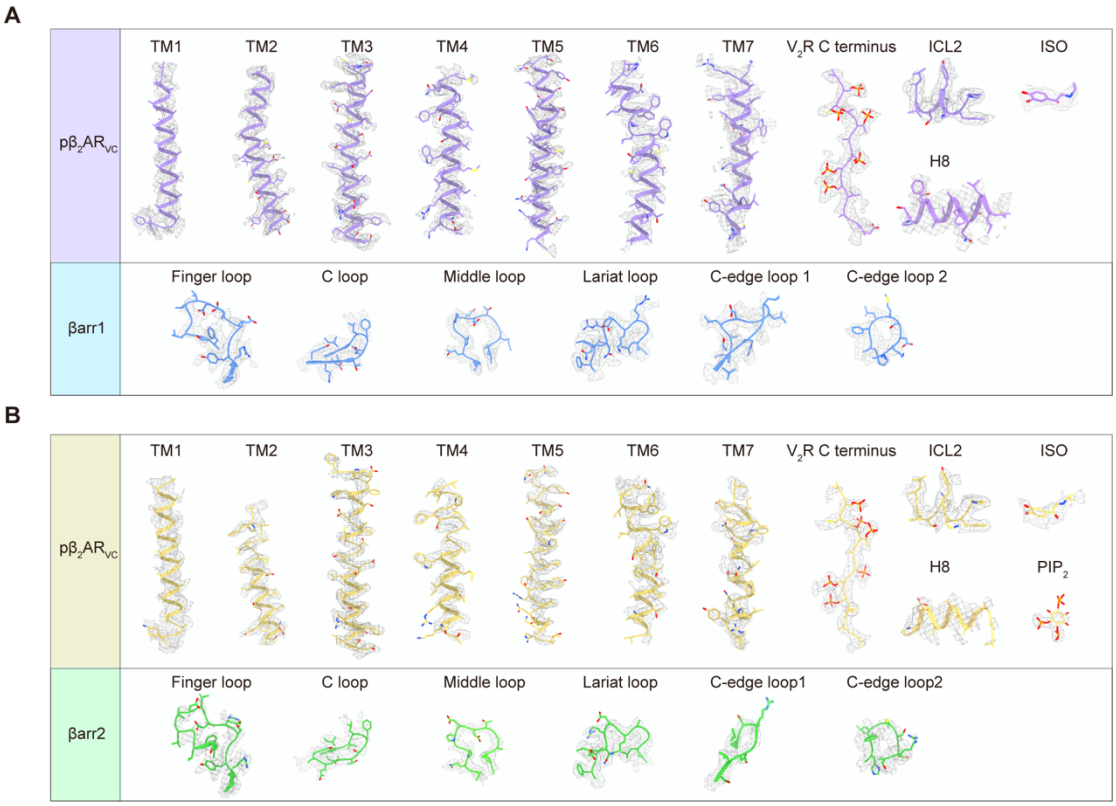

Fig. S10. Cryo-EM density maps with fitted models of the pβ$_2$AR$_{VC}$–βarr complexes. (**A**) pβ$_2$AR$_{VC}$–βarr1: cryo-EM density and fitted model are shown for β$_2$AR TM1–TM7, ICL2, H8, the V$_2$R C terminus, ISO (top) and for βarr1 central crest loops and C-edge loops (bottom). Density maps are shown in gray. (**B**) pβ$_2$AR$_{VC}$–βarr2: cryo-EM density and fitted model are shown for β$_2$AR TM1–TM7, ICL2, H8, the V$_2$R C terminus, ISO and PIP$_2$ (top), and for βarr2 central crest loops and C-edge loops (bottom). Density maps are colored grey.

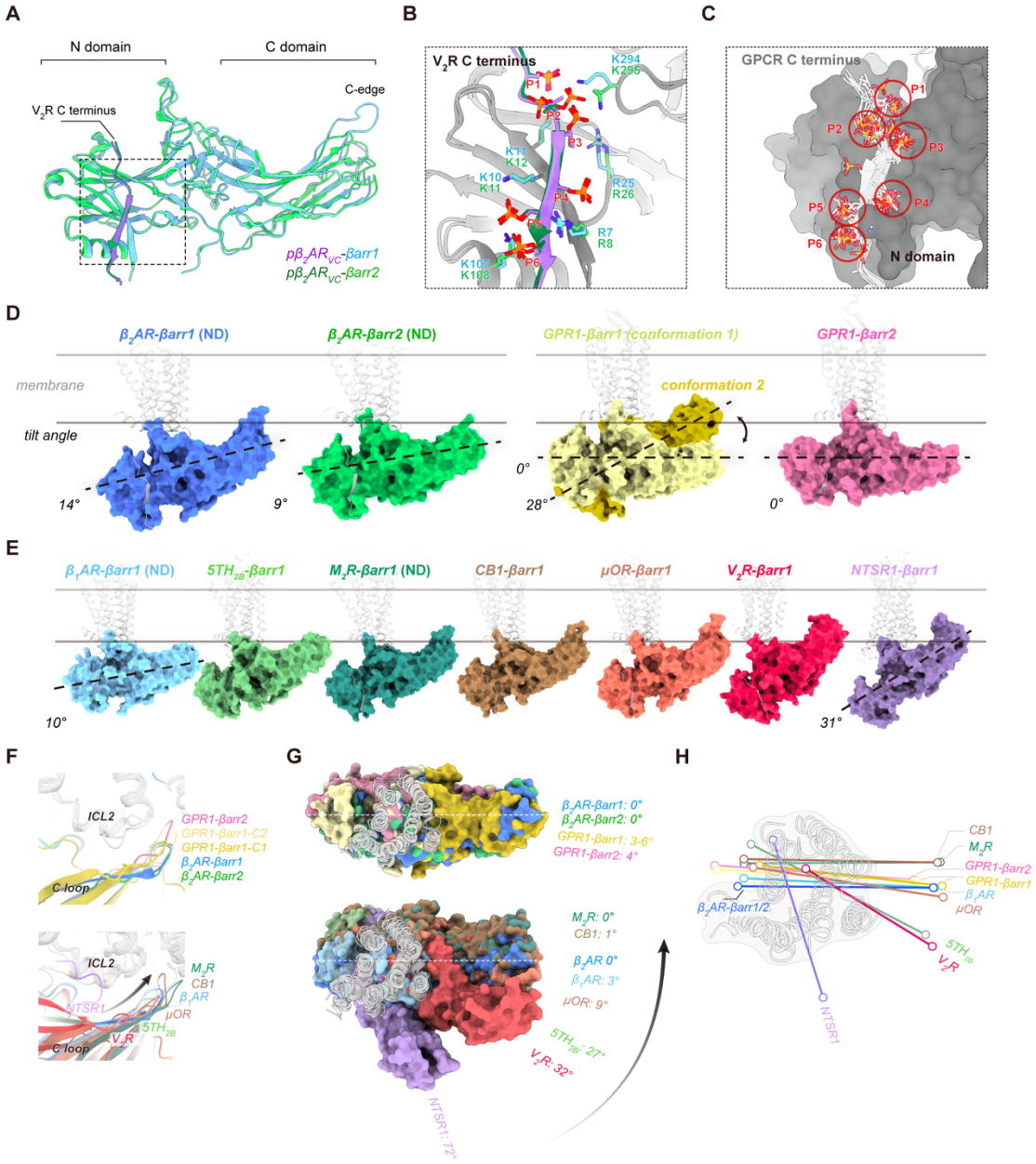

Fig. S11. Comparison of GPCR–βarr complex structures. (**A**) Overlay of the βarr structures in the pβ2ARVC–βarr1 (blue) and pβ2ARVC–βarr2 (green) complexes. (**B-C**) Local structures showing the resolved phosphate groups and their contacts with charged residues in βarr N domain observed in the pβ2ARVC–βarr1/2 structures (**B**), compared with other reported GPCR-arrestin complexes (PDB: 6U1N, 8JRV, 6TKO, 7R0C, 7SRS, 6UP7, 8WU1, 9WSV, 8TIO, 9UYH, 9UYL, 9UYM, **C**). (**D-E**) Tilt angle differences observed in the pβ2ARVC–βarr1/2 structures compared with the GPR1-βarr1/2 complexes (PDB: 9UYH, 9UYI, 9UYM) (**D**), and those observed in other GPCR–βarr1 complexes, including β1AR–βarr1 (PDB: 6TKO), 5TH2B–βarr1 (PDB: 7SRS), M2R–βarr1 (PDB: 6U1N), CB1–βarr1 (PDB: 8WU1), μOR–βarr1 (PDB: 9WSV), V2R–βarr1 (PDB: 7R0C), NTSR1–βarr1 (PDB: 6UP7) (**E**). The dashed line corresponds to the Cα–Cα vector between F149/F150 and L327/L328 of βarr1/2.

Structures determined in lipid nanodiscs (ND) are indicated. (**F**) Comparison of βarr C loop conformations in different GPCR–βarr complexes. The structures are aligned by the receptor chains. (**G**) Structural comparison with available GPCR–βarr complexes showing the differences of βarr docking orientation relative to the 7TM core viewed from the extracellular side. For clarity, comparison with the GPR1–βarr1/2 complexes are shown at the top, and comparison with other GPCR–βarr complexes are shown at the bottom. The structures are aligned by the receptor chains (gray), and the βarrs are shown as surface representations with different colors. The white dashed lines depict the Cα–Cα vector between βarr1 F149 and L327 (or βarr2 F150 and L328) residues in the $p\beta_2AR_{VC}$–βarr1/2 complex structures, which was used as the reference (0°) to define the in-plane rotation angle of βarrs relative to the 7TM core. (**H**) A simplified illustration showing both the differences in orientation angle and translational displacement of βarrs relative to the 7TM core in the GPCR–βarr complexes. The lines depict Cα–Cα vectors between F149/F150 and L327/L328 residues in βarr1/2.

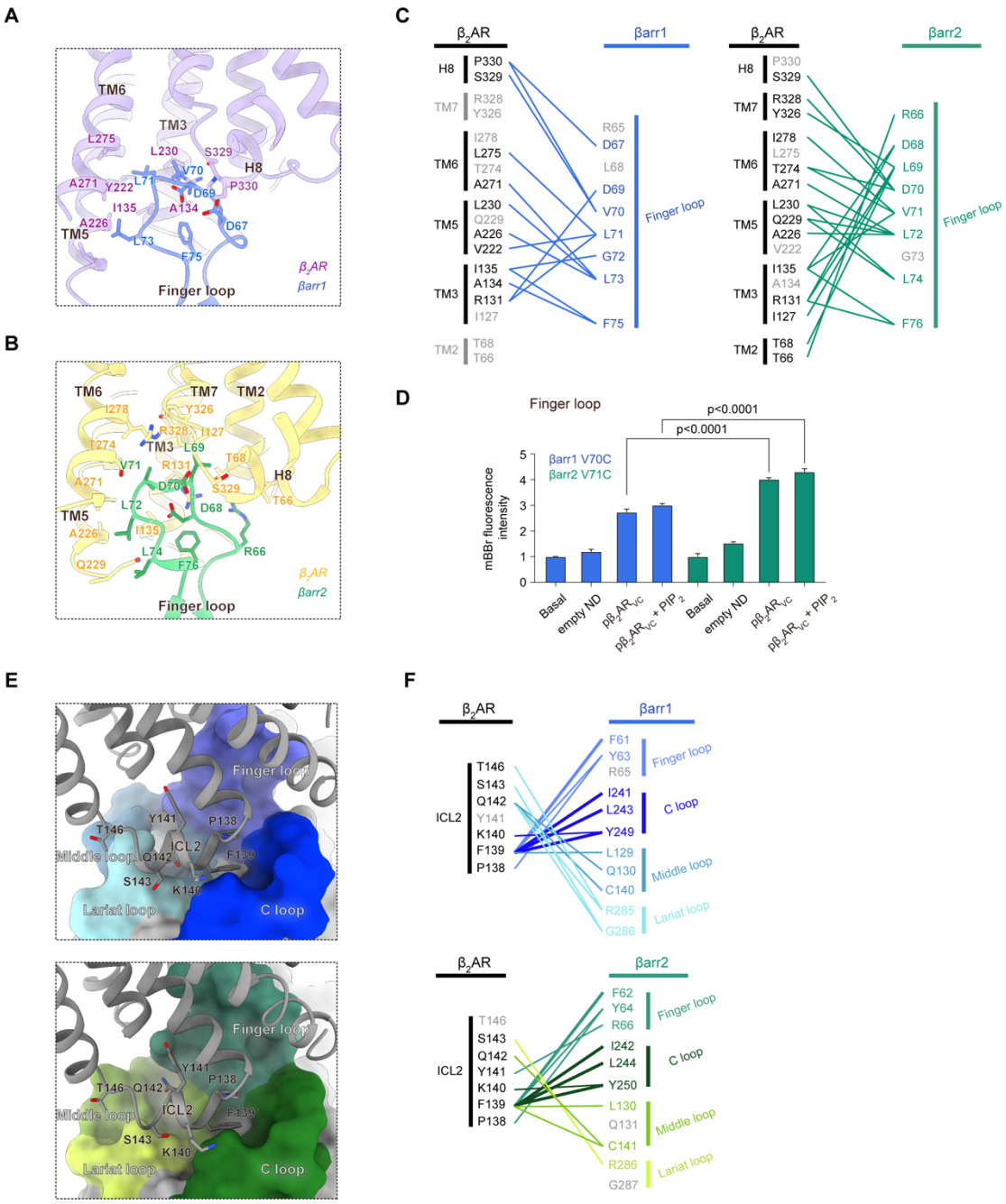

Fig. S12. Comparison of βarr1/2 central crest interactions with the β_2AR TM core. (**A-B**) Local structures showing the interactions of the βarr1 (**A**) and βarr2 (**B**) finger loops with the β_2AR TM core. Residues involved in the interactions are shown as sticks. (**C**) Contact maps between β_2AR TM core and βarr1/2 finger loops, defined by inter-residue heavy-atom distance cutoff of 4 Å. (**D**) Quantification of the mBBr fluorescence results reporting βarr finger loop (βarr1 V70C, βarr2 V71C) interactions with β_2AR TM core under different conditions. Compared with the data shown in Fig. 4H, two additional conditions (basal: inactive βarr in solution; pβ_2AR$_{VC}$+PIP$_2$: βarr in the presence of nanodisc-embedded pβ_2AR$_{VC}$ supplemented with PIP$_2$) were also included. Bars represent

fluorescence intensity quantified as the area under the curve (430–540 nm); n = 6 measurements from 3 independent experiments with 2 technical replicates each; data shown as mean ± SD. *P* values were obtained by two-way ANOVA with Šídák's multiple-comparisons test. (**E**) Detailed interactions between β_2AR ICL2 and the βarr central crest (top, βarr1; bottom, βarr2). Central crest loops are shown as surface representations, and ICL2 residues are shown as sticks. (**F**) Contact maps between β_2AR ICL2 and βarr central crest loops (top, βarr1; bottom, βarr2), using the same color code as in (**E**).

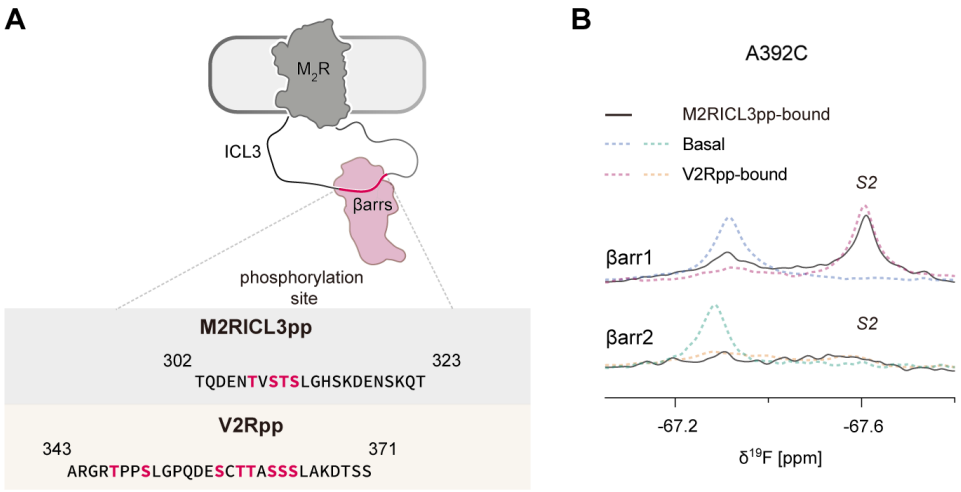

Fig. S13. C-tail conformations of βarr1 and βarr2 upon binding to a phosphopeptide derived from the M_2R ICL3 region. (**A**) A schematic illustration of βarrs binding to the ICL3 of M_2R in the hanging mode. The sequence of the synthesized peptide M2RICL3pp is shown at the bottom, together with that of V2Rpp. The phosphorylated sites in the peptides are colored in pink. (**B**) ^{19}F NMR spectra of the A392C site in both βarrs in the M2RICL3pp-bound state compared with the basal and V2Rpp-bound states.

Table S1. Cryo-EM data collection, refinement and validation statistics

	β_2AR_{VC}-βarr1	β_2AR_{VC}-βarr2
Data collection and processing		
Magnification	81,000	81,000
Voltage (kV)	300	300
Electron exposure ($e^-/Å^2$)	60	60
Defocus range (μm)	-1.0 ~ -1.5	-1.0 ~ -1.5
Pixel size (Å)	1.07	1.07
Symmetry imposed	C1	C1
Initial particle projections (no.)	6,125,640	42,132,418
Final particle projections (no.)	123,512	242,296
Map resolution (Å)	3.06	3.03
FSC threshold	0.143	0.143
Map resolution range (Å)	2.68 ~ 42.01	2.59 ~ 42.66
Refinement		
Initial model used	AlphaFold 3	β_2AR_{VC}-βarr1
Model resolution (Å)	3.21	3.16
FSC threshold	0.5	0.5
Map sharpening B factor ($Å^2$)	-84.5	-89.6
Model composition		
Non-hydrogen atoms	8,409	8,634
Protein residues	1,100	1,127
Ligands	1	2
B-factors ($Å^2$)		
Protein	12.12/155.16/72.33	20.48/148.45/67.73
Ligand	135.88/135.88/135.88	131.10/136.08/132.84
R.m.s. deviations		
Bond lengths (Å)	0.003	0.006
Bond angles (°)	0.606	0.749
Validation		
MolProbity score	1.86	2.23
Clashscore	10.20	14.79
Rotamer outliers (%)	0.00	0.22
Ramachandran plot		
Favored (%)	95.20	89.89
Allowed (%)	4.61	9.65
Disallowed (%)	0.19	0.46